國立交通大學
顯示科技研究所
碩士學位論文

藉由二氧化碳雷射加熱與張力拉伸產生
長週期光纖光柵之研究
Periodically Tapered Long-Period Fiber
Gratings by CO$_2$ Laser Heating and Tension
Stretching
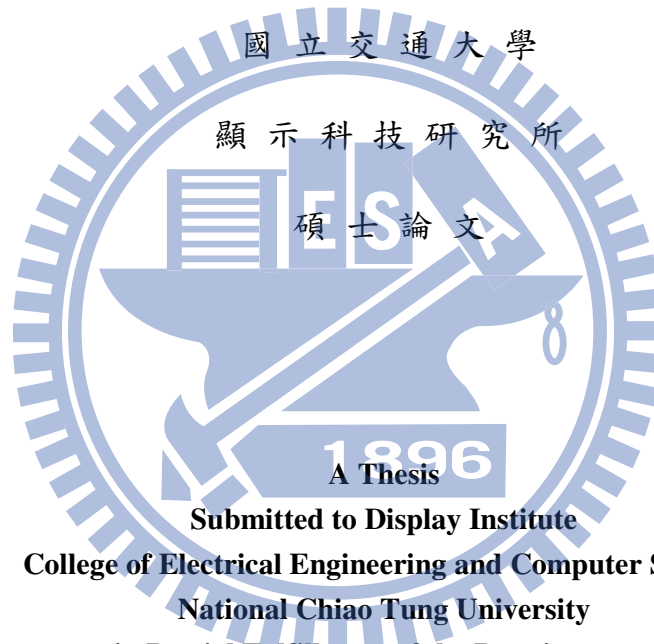
研究生：呂柏萱

指導教授：賴暎杰

中華民國九十九年六月

Periodically Tapered Long-Period Fiber Gratings by CO$_2$ Laser Heating and Tension Stretching

研 究 生：呂柏萱　　　　Student：Po-Hsuan Lu

指導教授：賴暎杰 老師　　Advisor：Yin-Chieh Lai

摘　要

論文名稱：藉由二氧化碳雷射加熱與張力拉伸製作長週期光纖光柵

校所別：國立交通大學顯示科技研究所　　　　頁數：1 頁

畢業時間：九十八學年度第二學期　　　　　　學位：碩士

研究生：呂柏萱　　　　　　　　　　　指導教授：賴暎杰 老師

關鍵詞：光纖濾波器、光纖感測器、熔拉、長週期光纖光柵

　　在本論文中，我們提出一種週期性熔錐形狀的長週期光纖光柵及製作方法。有別於以往二氧化碳雷射產生不對稱的長週期光纖光柵，我們產生的長週期光纖光柵是對稱的結構，而這個對稱的結構是藉由熔拉所產生。我們並藉由解三層結構光纖模態的數值模擬得到和實驗相吻合的結論。我們發現當週期性熔錐形狀明顯時，其對溫度的靈敏度升高。而將具週期性熔錐形狀光纖光柵置於較高折射率的介質中時，其對溫度的靈敏度亦升高。

　　具週期性熔錐形狀光纖光柵的製作方法如下：首先將高功率的二氧化碳雷射經過柱狀透鏡聚焦後加熱光纖，此光纖的一端固定而另一端則懸掛重物(重物即為光纖所受到的張力)，熔融的光纖經張力拉伸後產生熔拉的形狀。將上述光纖裝置於一個移動平台上，並用一個開關去控制二氧化碳雷射的加熱的時間。我們利用 Labview 進行自動控制，藉由控制開關打開的時間可以決定加熱的時間，藉由移動平台的移動的距離可以決定光柵的週期。此對稱光纖光柵對溫度的靈敏度(週期為 700 μm 且拉伸後的直徑 100 μm 的樣本)測得為 0.238 nm/℃，比傳統的 0.059 nm/℃ 改善很多。

ABSTRACT

Title：Periodically Tapered Long-Period Fiber Gratings by CO_2 Laser Heating and Tension Stretching

Pages：1 Page

School：National Chiao Tung University

Department：Display Institute

Time：June, 2010   Degree：Master

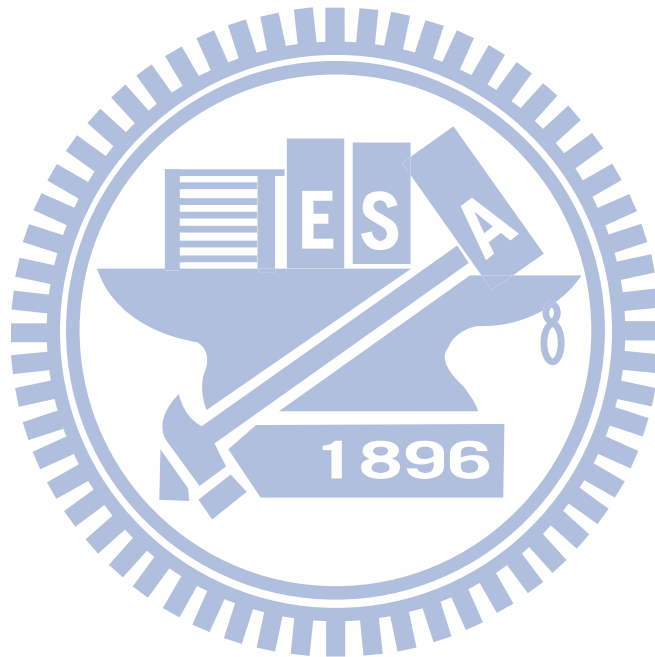Researcher：Po-Hsuan Lu   Advisor：Prof. Yin-Chieh Lai

Keywords： Fiber filter、Fiber sensor、Taper、Long period fiber grating

  In this thesis, we demonstrate a periodically tapered long period fiber grating and its fabrication method. Not as the same as the asymmetric long period fiber gratings produced before, we have produced devices with a symmetric structure tapered by a CO_2 Laser. The produced LPFG with deep corrugated surface structure and immersed in higher index media results in high temperature sensitivity. The numerical results performed by solving waveguiding modes in three-layer optical fibers agree with the experimental observation.

  The procedure of making a periodically tapered long period fiber grating is as following: First, let the high power CO_2 laser beam pass through the cylindrical lens and focused on the fiber, which is fixed at one end and tagged with a weight at the other end (the stress of the fiber equals the weight). Then, the melting fiber will be extruded and shaped like a tapered fiber with laser heating. The fiber is put on a translation stage and a shutter is used to control

the heating time of the CO_2 laser. We use the Labview software to control the translation stage and the shutter automatically so that we can set the parameters like the heating time and period easily. This kind of symmetric long period fiber gratings is more sensitive to temperature. We have measured the temperature sensitivity 0.238 nm/˚C for one of our LPFG samples, which is much better than the temperature sensitivity of traditional long period fiber gratings (0.059 nm/˚C).

ACKNOWLEDGEMENT

CONTENTS

LIST OF FIGURES

Chapter 1

Introduction

1.1 Introduction of Fiber Gratings

Fiber gratings are fiber devices that have already found many applications in optical communication and optical sensing. They can be classified according to the grating periods into two types, fiber Bragg gratings (also called reflection and short-period fiber gratings, denoted as FBGs) and long-period fiber gratings (also called transmission gratings, denoted as LPFGs). The periods of FBGs are normally under one micron meter while the periods of LPFGs are usually several hundred micron meters. In this thesis, we use a CO_2 laser to fabricate LPFGs. Because the focused CO_2 laser beam size is much larger than one micron meter, we can't fabricate FBGs using our experimental setup. However, the CO_2 laser is quite suitable for fabricating new kinds of LPFGs.

1.1-1 Various Fabrication Methods

Fiber gratings are first produced by exposing an optical fiber to ultra-violet (UV) lights that perturb the refractive index of the core to form a periodic index modulation profile. The photosensitive phenomenon in optical fibers was first demonstrated by Hill el al. in 1978 [1-1]. Here photosensitive means that the refractive index of certain doped glass can be raised by the exposure of UV lights. The magnitude of the refractive index change depends on the exposure time and dopant density (such as Germania) in the fiber and is typically between 10^{-6} and 10^{-3}. The dopants are usually doped only in the core of fibers, so that the UV induced index change is only in the core, not in the cladding of

fibers. By using the techniques such as hydrogen loading, an index change as high as 10^{-2} can be obtained.

Since the period of fiber Bragg gratings are usually under one micron meter, the only way to fabricate such a short period grating is by utilizing either an interferometer or a phase mask to perform UV exposure. The transverse holographic method was first proposed by Meltz et al [1-2] in 1989. The UV interference pattern is imposed on the fiber from the side as shown in figure 1.1. After a few years, the phase mask technique [1-3]-[1-5] as shown in figure 1.2 became widely used to simplify the fabrication procedure and to more easily produce fiber gratings with high performance. In order to fabricate long and complex fiber gratings with advanced characteristics, the systems of sequential writing have also been proposed and demonstrated [1-6]-[1-8].
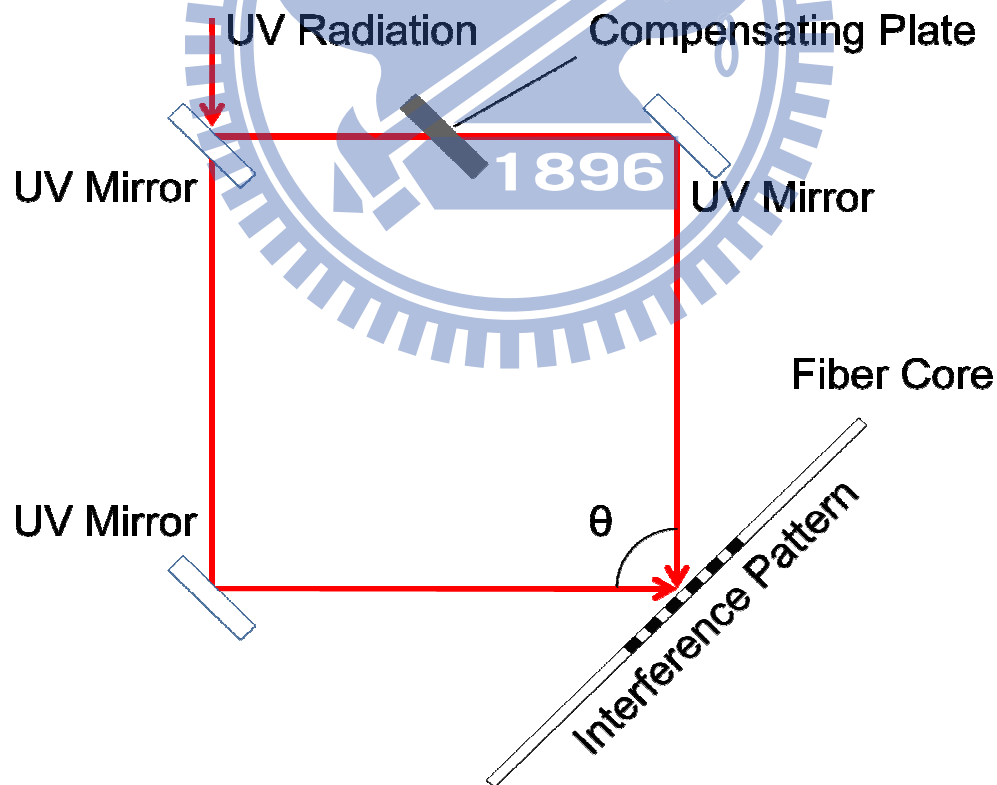
Fig. 1.1 Two coherent UV beams produce an interference pattern in the fiber. The period of the grating depends on the angle θ of the two incident beams.
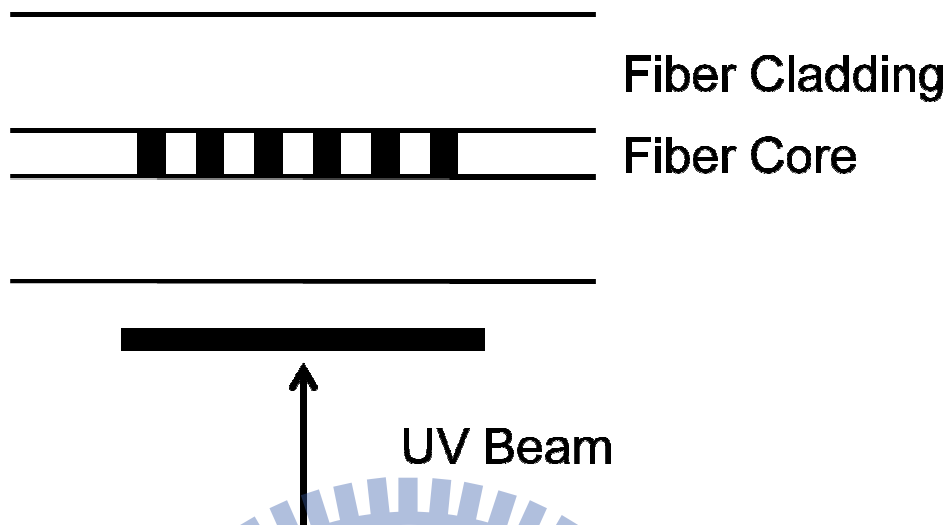
Fig. 1.2 The fiber grating is fabricated by a UV beam incident to a phase mask (PM). The period of the fiber grating is half of the PM period.

On the contrary, LPFGs have larger period than FBGs. UV illumination is just one of the methods. In addition, LPFGs have also been designed and realized by thermally induced methods such as the use of a CO_2 laser [1-9] and arc discharge with a conventional splicer [1-10]. These methods are cheaper and more available than UV photo-imprinting method.

1.1-2 Characteristics

FBGs couple the fundamental core mode to the mode of the reverse traveling direction. To inspect a fiber Bragg grating, we can observe the reflection spectrum while the LPFGs only the core couple to the co-propagated cladding mode which can only be observed in the transmission spectrum. Figure1.3 shows the conventional reflection spectrum of FBGs. Figure1.4 shows the conventional transmission spectrum of LPFGs.
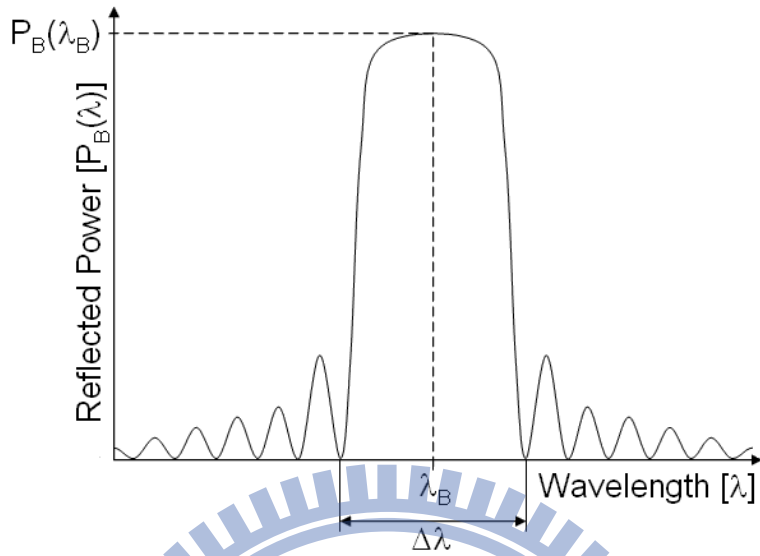
Fig. 1.3 Conventional reflection spectrum of FBGs.
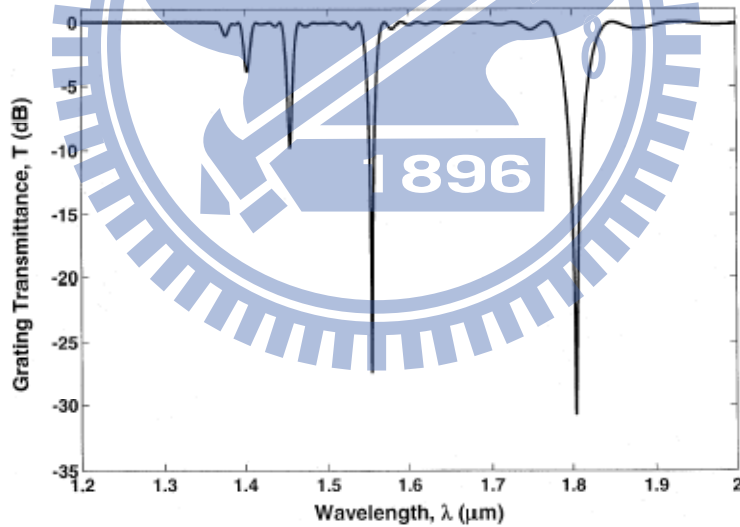
Fig. 1.4 Conventional transmission spectrum of LPFGs.

1.1-3 Applications

Long-period fiber gratings have been developed into a crucial optical component in many applications. They are used in optical communication

- 4 -

systems such as low-loss in-fiber band rejection filters [1-11], gain-flattening devices in erbium-doped fiber amplifiers (EDFAs) [1-12], highly sensitive optical fiber sensors, selective mode converters, and polarization-selective devices. They may provide options to the network designers that should influence, for example, the deployment of wavelength-division-multiplexed (WDM) systems, channel selection, and deployment of transmitters in the upstream path in a network, and should make routing viable.

In sensing applications, the conventional LPFGs have limited wavelength sensitivity of temperature and refractive index due to the tight mode field confinement. Numerous kinds of LPFGs have been proposed to enhance the sensitivity, including the short-grating period [1-13], ultra-thin cladding layer [1-14], asymmetric CO_2 laser ablation [1-15]-[1-17], surface-corrugated fiber [1-18].

1.2 Motivation of the thesis

1.2-1 Previous Work

In the previous work, our lab had produced two kinds of asymmetric long-period fiber gratings. Our first kind of long-period fiber grating is with surface corrugated structure which was ablated by focused CO_2 laser[1-18]. Our second kind of long-period fiber gratings is produced by using a metal grating side-contacted on tapered fiber[1-19]. The lack of structure symmetry on the fiber cross section may cause asymmetry mode profiles and complicated mode coupling, and exhibit polarization-dependent losses. In particular, since the asymmetric structure is polarization dependent, this may cause some problems the resonance dips not sharp enough for practical

sensing applications.

1.2-2 Motivation

We want to make a highly symmetric long-period fiber grating which is theoretically polarization independent. So we choose a cylindrical lens instead of a circular lens to assure the heating area is more symmetrical along with respect to the fiber axis. Since it has the waveguide structure to let the cladding modes spread more out of the fiber, we predict it can be highly sensitive to the environmental fluctuations. This means that it can be utilized as a sensor device for different applications.

1.3 Structure of the thesis

The present thesis comprises four chapters. Chapter 1 is an introductory chapter consisted of an introduction to fiber gratings and the motivation of our research. Chapter 2 describes the principles and analysis of our research work. We use a three-layer waveguide to calculate the mode refractive indices, which can be used to predict the coupling wavelength of the LPFG. Chapter 3 describes our experimental procedures, and shows the measurement results. Finally, chapter 4 gives the conclusions and discusses possible future works.

1.4References

[1-1] K. O. Hill, Y. Fujii, D. C. Johnson, and B. Kawasaki, "Photosensitivity in Optical Fiber Waveguides : Application to Reflection Fiber Fabrication, " Appl. Phys. Lett. 32(10), p647(1978).

[1-2] G. Meltz, W. W. Morey, and W. H. Glenn, "Formation of Bragg gratings in optical fibers by a transverse holographic method, " Opt. Lett. 14, 823-825

(1989).

[1-3] M. Gagné, L. Bojor, R. Maciejko, and R. Kashyap, "Novel custom fiber Bragg grating fabrication technique based on push-pull phase shifting interferometry, " Opt. Express 16, 21550-21557 (2008).

[1-4] J. Albert, K. O. Hill, B. Malo, S. The´riault, F. Bilodeau, D.C. Johnson and L.E. Erickson, "Apodization of the spectral response of fiber Bragg gratings using a phase mask with variable diffraction efficiency," Electron. Lett. 31, 222, (1995).

[1-5] W. H. Loh, M. J. Cole, M. N. Zervas, S. Barcelos, and R. I. Laming, "Complex grating structures with uniform phase masks based on the moving fiber-scanning beam technique, " Opt. Lett. 20, 2051-2053 (1995).

[1-6] J. B. Jensen, N. Plougmann, H.-J. Deyerl, P. Varming, J. Hubner, and M. Kristensen, "Polarization control method for ultraviolet writing of advanced Bragg gratings, "Opt. Lett. 27, 1004-1006 (2002).

[1-7] A. Asseh, H. Storoy, Bengt E. Sahlgren, S. Sandgren, and Raoul A. H. Stubbe, "A writing technique for long fiber Bragg gratings with complex reflectivity profiles," Journal of Lightwave Technology, vol. 15, pp.1419-1423, (1997).

[1-8] I. Petermann, B.Sahlgren, S. Helmfrid, A. T. Friberg, and P.-Y. Fonjallaz, "Fabrication of Advanced Fiber Bragg Gratings by use of Sequential Writing with a Continuous-Wave Ultraviolet Laser Source, " Appl. Opt. 41, 1051-1056 (2002).

[1-9] D. D. Davis, T. K. Gaylord, E. N. Glytsis, S. G. Kosinski, S. C. Mettler, and A. M. Vengsarkar, "Long period fiber grating fabrication with focused CO_2 laser beams," Electron. Lett. 34, 302-303 (1998).

[1-10] A. Malki, G. Humbert, Y. Ouerdane, A. Boukhenter, and A. Boudrioua,

"Investigation of the Writing Mechanism of Electric-Arc-Induced Long-Period Fiber Gratings," Appl. Opt. 42, 3776-3779 (2003).

[1-11] A.M. Vengsarkar, P.J. Lemaire, J.B. Judkins, V. Bhatina, T. Erdogan and J.E. Sipe, "Long-period fiber gratings as band-rejection filter, " IEEE J. Lightwave Technol. 14, 58–65(1996).

[1-12] A. M. Vengsarkar, J. R. Pedrazzani, J. B. Judkins, P. J. Lemaire, N. S. Bergano and, C. R. Davidson, "Long- period fiber-grating-based gain equalizers, " Opt. Lett. 21, 336-338 (1996).

[1-13] H. J. Patrick, A. D. Kersey, and F. Bucholtz, "Analysis of the Response of Long Period Fiber Gratings to External Index of Refraction, " J. Lightwave Technol. 16, 1606- (1998).

[1-14] K.-W. Chung and S. Yin, "Analysis of a widely tunable long-period grating by use of an ultrathin cladding layer and higher-order cladding mode coupling, " Opt. Lett. 29, 812-814 (2004).

[1-15] M. Yan, S. Luo, L. Zhan, Z. Zhang, and Y. Xia, "Triple-wavelength switchable Erbium doped fiber laser with cascaded asymmetric exposure long-period fiber gratings, "Opt. Express 15, 3685-3691 (2007)

[1-16] Y. Rao and T. Zhu, " A Highly Sensitive Fiber-Optic Refractive Index Sensor Based on an Edge-Written Long-Period Fiber Grating, " in Nonlinear Photonics, OSA Technical Digest (CD) ,paper JWA53 (Optical Society of America,(2007).

[1-17] N.-K. Chen, D.-Y. Hsu, and S. Chi, "Widely tunable asymmetric long-period fiber grating with high sensitivity using optical polymer on laser-ablated cladding, " Opt. Lett. 32, 2082-2084 (2007).

[1-18] W. Ding and S. R. Andrews, "Modal coupling in surface-corrugated long-period-grating fiber tapers, " Opt. Lett. 33, 717-719 (2008).

[1-19] K.-C. Hsu, N.-K. Chen, C.-L. Lee, Y.-S. Chih, P.-J. Jhuang, Y. Lai, and C. Lin, "Spectral Response of Long-Period Fiber Grating Based on Tapered Fiber With Side-Contacted Metal Grating, " J. Lightwave Technol. 28, 1057-1063 (2010).

Chapter2
Theory

In this chapter we will introduce the phase-matching condition and coupled-mode theory at first. Then we use a uniform waveguide model, which contained three layers of media, including core, cladding, and surrounding medium, to derive boundary conditions at the interfaces. With the boundary conditions, we can get the propagating conditions of the waveguide. By solving the waveguide propagating conditions, we can calculate the effect refractive indices of the fundamental core mode and higher order cladding modes propagating in the waveguide with different incident wavelengths. Combining the phase-matching condition and the effective refractive indices calculated by the model, we can figure out how resonance wavelength change as the temperature increases or the surrounding medium is changed. In order to simulate broad band transmission spectrum of LPFGs, we should also consider the material dispersion. So we will also introduce the dispersion mechanism at last.

2.1 Phase-matching condition

Figure 2.1 shows a light-wave diffracted by a fiber grating. A light-wave incident into the grating at an angle θ_1 can be described by the grating equation

$$n\sin\theta_2 = n\sin\theta_1 + m\frac{2\pi}{\lambda} \tag{2.1}$$

where θ_2 is the angle of the diffracted wave and the integer m is the diffraction order.
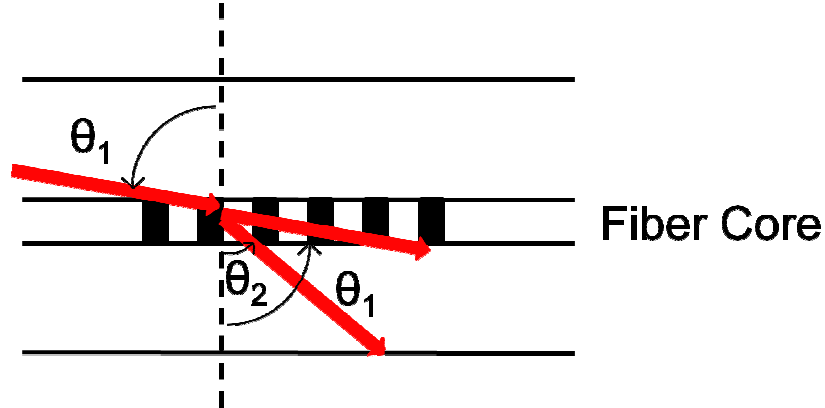
Fig. 2.1 A light-wave diffracted by a fiber grating.

Equation (2.1) is able to determine the wavelength at which a fiber grating can most efficiently couple lights between two modes. We can even know the coupling direction by θ_2.

For Bragg gratings, θ_2 is negative, and the coupling occurs between modes traveling in opposite directions; for transmission gratings, θ_2 is positive, the coupling is between modes traveling in the same direction. Since the mode propagation constant β is simply $\beta = (2\pi/\lambda)n_{eff}$, where $n_{eff} = n_{co}\sin\theta$, we may rewrite for guided modes as

$$\beta_2 = \beta_1 + m\frac{2\pi}{\Lambda} \ . \tag{2.2}$$

For example, first-order reflective diffraction usually dominates in a fiber Bragg grating, m=-1. Positive and negative β values describe modes that propagate in the +z and –z direction, respectively. The physical meaning is the phase-matching condition, and the schematic diagram can be shown as figure 2.2.
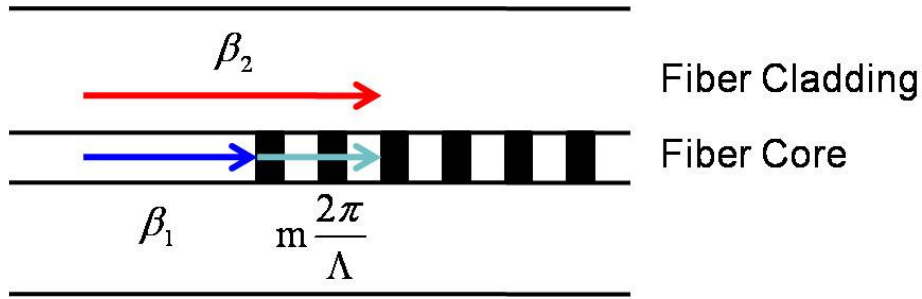
Fig. 2.2 The schematic diagram of phase-matching condition.

By using equation (2.2) and recognizing $\beta_2<0$, we find that the resonant wavelength for the reflection of a mode of index $n_{eff,1}$ into another mode of index $n_{eff,2}$ is

$$m\lambda = \left(n_{eff,1} + n_{eff,2}\right)\Lambda. \tag{2.3}$$

If the two modes are identical, i.e. $n_{eff,1} = n_{eff,2} = n_{eff}$, we get the familiar result for Bragg reflection：

$$m\lambda = 2n_{eff}\Lambda. \tag{2.4}$$

When light is diffracted by a transmission grating, the first mode is a core mode while the second one is a cladding mode. Since here $\beta_2>0$, the resonant wavelength for a transmission grating is

$$m\lambda = (n_{eff,1} - n_{eff,2})\Lambda. \tag{2.5}$$

2.2 Coupled-mode theory

In the following derivation, for simplicity a perturbation applied to the core refractive index n_{co} will be described by [9]

$$\Delta n_{co}(z) = \overline{\Delta n}_{co}(z)\{1 + v\cos\left[\frac{2\pi}{\Lambda}z + \phi(z)\right]\} \tag{2.6}$$

where $\overline{\Delta n}_{co}(z)$ is the dc index change spatially averaged over a grating period,

v is the fringe visibility of index change, Λ is the grating period, and $\phi(z)$ describes the grating phase.

Since the long-period fiber grating couples the forward propagating guided core mode of amplitude $A_1(z)$ to one of the co-propagating cladding modes of amplitude $A_2(z)$, the coupled-mode equations of long-period fiber grating can be written as

$$\frac{dA^{co}(z)}{dz} = i\hat{\sigma}A^{co}(z) + i\kappa(z)A^{cl}(z) \tag{2.7}$$

$$\frac{dA^{cl}(z)}{dz} = i\hat{\sigma}A^{cl}(z) + i\kappa^*(z)A^{cl}(z) \tag{2.8}$$

where the amplitudes $A^{co}(z)$ and $A^{cl}(z)$ are

$$A^{co}(z) \equiv A_1(z) \exp\left[-\frac{i(\sigma_{11}+\sigma_{22})z}{2}\right] \exp\left(i\delta z - \frac{\phi}{2}\right) \tag{2.9}$$

$$A^{cl}(z) \equiv A_2(z) \exp\left[-\frac{i(\sigma_{11}+\sigma_{22})z}{2}\right] \exp\left(-i\delta z + \frac{\phi}{2}\right) \tag{2.10}$$

, and σ_{11}, σ_{22} are dc coupling coefficients defined in

$$\sigma_{kj}(z) = \frac{\omega n_{co}}{2}\overline{\Delta n_{co}}(z) \iint_{core} \overrightarrow{\varepsilon_{kt}}(x,y) \cdot \overrightarrow{\varepsilon_{jt}^*}(x,y)dxdy \tag{2.11}$$

The mode coupling coefficient functions are defined as

$$\kappa_{kj}(z) = \frac{v}{2}\sigma_{kj}(z) \qquad k,j=1,2 \tag{2.12}$$

where $\overrightarrow{\varepsilon_{jt}}(x,y)$ are transverse mode fields. When j is equal to 1, it refers to the core mode. When j is equal to 2, it describes the cladding mode.

$\kappa = \kappa_{21} = \kappa_{12}^*$ is the ac cross-coupling coefficient and $\hat{\sigma}$ is the dc self-coupling coefficient defined as

$$\hat{\sigma} \equiv \delta + \frac{\sigma_{11}-\sigma_{22}}{2} - \frac{1}{2}\frac{d\phi}{dz}. \tag{2.13}$$

Here the detuning, which is assumed to be constant along z, is

$$\delta \equiv \frac{1}{2}(\beta^{co} - \beta^{cl}) - \frac{\pi}{\Lambda} = \pi\Delta n_{co}(\frac{1}{\lambda} - \frac{1}{\lambda_D}). \tag{2.14}$$

Here β^{co} and β^{cl} are the propagation constants related to the core and

cladding modes, $\lambda_D \equiv \Delta n_{co} \Lambda$ is the design wavelength for an infinitesimally weak grating, Δn_{co} is the difference of the core and the cladding effective indices, and Λ is the period of the long-period fiber grating. When appropriate initial conditions $A^{co}(0) = 1$ and $A^{cl}(0) = 0$ are specified, closed form solutions can be found. The core mode and the cladding mode transmission coefficients for uniform long-period fiber gratings can be shown to be

$$T_{co} = \left| \frac{A^{co}(L)}{A^{co}(0)} \right|^2 = \cos^2 \left(\sqrt{\kappa^2 + \hat{\sigma}^2} z \right) + \frac{\hat{\sigma}^2}{\kappa^2 + \hat{\sigma}^2} \sin^2 \left(\sqrt{\kappa^2 + \hat{\sigma}^2} z \right)$$

(2.15)

$$T_{cl} = \left| \frac{A^{cl}(L)}{A^{co}(0)} \right|^2 = \frac{\kappa^2}{\kappa^2 + \hat{\sigma}^2} \sin^2 \left(\sqrt{\kappa^2 + \hat{\sigma}^2} z \right) \qquad (2.16)$$

2.3 Wave guiding conditions

Figure 2.3 depicts the fiber structure considered as a three-layer waveguide, including core, cladding, and the surrounding medium of the fiber.
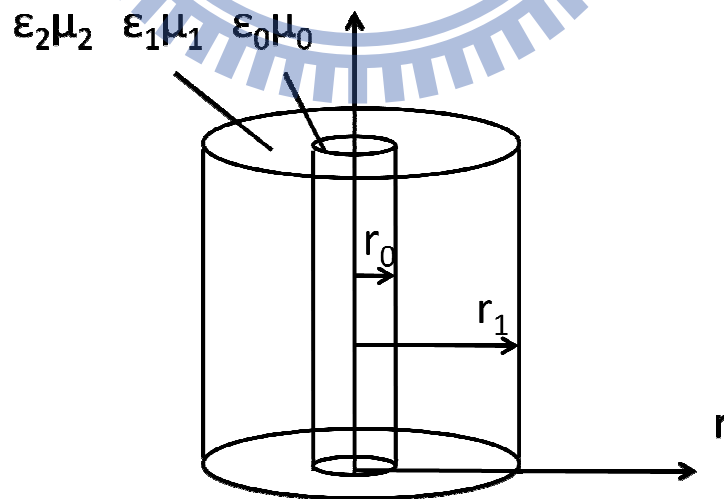
Fig. 2.3 Step profile of three layer fiber.

The modes of such a straight fiber are approximations to the solutions of Maxwell's equations within local regions of the LPFGs. The variables r_0 and r_1 are the radius of the core and cladding. The core with constitutive parameters μ_0 and ε_0 is embedded in the cladding with μ_1 and ε_1, which is surrounded by the external medium with μ_2 and ε_2. The field distributions and propagation constants of the modes can be obtained by solving the appropriate boundary-value problem of the wave-guiding equations. The wave-guiding equation for longitudinal components of the fields (E_z and H_z) in the cylindrical polar coordinates (r, φ, z) with the z-axis along the axis of the fiber is given by

$$\left[\frac{1}{r}\frac{\partial}{\partial r}\left(r\frac{\partial}{\partial r}\right) + \frac{1}{r}\frac{\partial^2}{\partial \varphi^2} + k_r^2\right]\begin{Bmatrix}E_z\\H_z\end{Bmatrix} = 0 \tag{2.17}$$

where $k_r^2 = \omega^2\varepsilon\mu - k_z^2$.

Inside the core, solutions for E_z and H_z are Bessel functions, which are given by

$$E_z = AJ_m(k_{r0}r)\cos(m\varphi)\exp(ik_z z) \tag{2.18}$$

$$H_z = BJ_m(k_{r0}r)\sin(m\varphi)\exp(ik_z z) \tag{2.19}$$

with $k_z^2 + k_{r0}^2 = \omega^2\varepsilon_0\mu_0$.

In the cladding region, solutions for E_z and H_z are

$$E_z = CJ_m(k_{r1}r)\cos(m\varphi)\exp(ik_z z) + DY_m(k_{r1}r)\cos(m\varphi)\exp(ik_z z) \tag{2.20}$$

$$H_z = FJ_m(k_{r1}r)\sin(m\varphi)\exp(ik_z z) + GY_m(k_{r1}r)\sin(m\varphi)\exp(ik_z z) \tag{2.21}$$

with $k_z^2 + k_{r1}^2 = \omega^2\varepsilon_1\mu_1$.

In the surrounding, the field associated with the guiding wave is evanescent in the radial direction. By letting $k_{r1} = i\alpha_{r2}$, the solutions in the surrounding are

$$E_z = IH_m^{(1)}(i\alpha_{r2}r)\cos(m\varphi)\exp(ik_z z) \tag{2.22}$$

$$H_z = JH_m^{(1)}(i\alpha_{r2}r)\sin(m\varphi)\exp(ik_z z) \tag{2.23}$$

with $k_z^2 + k_{r2}^2 = \omega^2\varepsilon_2\mu_2$.

In the aforementioned solutions, J_m and Y_m are the Bessel functions of the first and second kind, respectively, and $H_m^{(1)}$ is the Hankel function. There are eight coefficients A, B, C, D, F, G, I, and J, and to be solved by boundary conditions at interfaces between different dielectric media. The following four equations at $r = r_0$ are obtained:

$$AJ_m(k_{r_0}r_0) - CJ_m(k_{r_1}r_0) - DY_m(k_{r_1}r_0) = 0 \tag{2.24}$$

$$BJ_m(k_{r_0}r_0) - FJ_m(k_{r_1}r_0) - GY_m(k_{r_1}r_0) = 0 \tag{2.25}$$

$$A\frac{\omega\varepsilon_0}{k_{r_0}r_0}J'_m(k_{r_0}r_0) + B\frac{mk_z}{k_{r_0}^2 r_0^2}J_m(k_{r_1}r_0) - C\frac{\omega\varepsilon_1}{k_{r_1}r_0}J'_m(k_{r_1}r_0) - D\frac{\omega\varepsilon_1}{k_{r_1}r_0}Y'_m(k_{r_1}r_0) -$$

$$F\frac{mk_z}{k_{r_1}^2 r_0^2}J_m(k_{r_1}r_0) - G\frac{mk_z}{k_{r_1}^2 r_0^2}Y_m(k_{r_1}r_0) = 0 \tag{2.26}$$

$$A\frac{mk_z}{k_{r_0}^2 r_0^2}J_m(k_{r_0}r_0) + B\frac{\omega\mu_0}{k_{r_0}r_0}J'_m(k_{r_0}r_0) - C\frac{mk_z}{k_{r_1}^2 r_0^2}J_m(k_{r_1}r_0) - D\frac{mk_z}{k_{r_1}^2 r_0^2}Y_m(k_{r_1}r_0) -$$

$$F\frac{\omega\mu_1}{k_{r_1}r_0}J'_m(k_{r_1}r_0) - G\frac{\omega\mu_1}{k_{r_1}r_0}Y'_m(k_{r_1}r_0) = 0 \tag{2.27}$$

and the other four are obtained from boundary conditions at $r = r_1$, as

$$CJ_m(k_{r_1}r_1) + DY_m(k_{r_1}r_1) - IH_m(i\alpha_{r_2}r_1) = 0, \tag{2.28}$$

$$FJ_m(k_{r_1}r_1) + GY_m(k_{r_1}r_1) - JH_m(i\alpha_{r_2}r_1) = 0, \tag{2.29}$$

$$C\frac{\omega\varepsilon_1}{k_{r_1}r_1}J'_m(k_{r_1}r_1) + D\frac{\omega\varepsilon_1}{k_{r_1}r_1}Y'_m(k_{r_1}r_1) + F\frac{mk_z}{k_{r_1}^2 r_1^2}J_m(k_{r_1}r_1) + G\frac{mk_z}{k_{r_1}^2 r_1^2}Y_m(k_{r_1}r_1) +$$

$$I\frac{i\omega\varepsilon_2}{\alpha_{r_2}r_1}H'_m(i\alpha_{r_2}r_1) + J\frac{mk_z}{\alpha_{r_2}^2 r_1^2}H_m(i\alpha_{r_2}r_1) = 0 \tag{2.30}$$

$$C\frac{mk_z}{k_{r_1}^2 r_1^2}J_m(k_{r_1}r_1) + D\frac{mk_z}{k_{r_1}^2 r_1^2}Y_m(k_{r_1}r_1) + F\frac{\omega\mu_1}{k_{r_1}^2 r_1^2}J'_m(k_{r_1}r_1) + G\frac{\omega\mu_1}{k_{r_1}^2 r_1^2}Y'_m(k_{r_1}r_1) +$$

$$I\frac{mk_z}{\alpha_{r_2}^2 r_1^2}H'_m(i\alpha_{r_2}r_1) + J\frac{i\omega\mu_2}{\alpha_{r_2}r_1}H'_m(i\alpha_{r_2}r_1) = 0 \tag{2.31}$$

Equations (2.24)–(2.31) resulted from the continuity of E_z, H_z, and E_φ, H_φ give rise to the guidance conditions for the waveguide modes. Since the eight equations are a set of homogeneous linear equations, the determinant of the coefficient matrix has to be zero in order to have nonzero solutions. This condition is the final characteristic equation for determining the dispersion

relation of the modes.

2.4 Dispersion Mechanism

The dispersion property is important for determining the spectral characteristics of a fiber filter component with its evanescent wave interacted with the environment. The causes of dispersion can be divided into two categories, material and waveguide dispersion. In general, the material dispersion comes from the material dispersion properties of the fiber material and the external medium while the waveguide dispersion results from the waveguiding fiber structure. For the filter fiber devices studied here, the relative refractive index difference of the fiber waveguide changes with the variation of wavelength through the material and waveguide dispersion. Therefore, the spectral responses will also vary accordingly.

These influences are important when a wide range of wavelengths are considered.

2.4-1 Material Dispersion

The material dispersion is defined as the variation of refractive index with the wavelength of light. The material dispersion of glass can be expressed by Sellmeier equation. The formula is valid at frequencies far from material resonance:

$$n^2 - 1 = \sum_{j=1}^{p} \frac{A_j \lambda^2}{\lambda^2 - \lambda_j^2} \tag{2.32}$$

The summation is taken over all the resonance wavelengths. For silica, a three-term Sellmeier equation is typically used, accounting for the resonances in the ultraviolet and infrared:

$$n^2 - 1 = \frac{A_1\lambda^2}{\lambda^2 - \lambda_1^2} + \frac{A_2\lambda^2}{\lambda^2 - \lambda_2^2} + \frac{A_3\lambda^2}{\lambda^2 - \lambda_3^2} \qquad (2.33)$$

Equation (2.42) is plotted in figure 2.4 for pure silica and for 4.1% Germania-doped silica, using the empirically determined Sellmeier coefficients given in Table 2.1[2.1-2.2].

Material	A1	λ(μm)	A2	λ(μm)	A3	λ(μm)
SiO$_2$ [1.17]	0.6961663	0.0684043	0.4079426	0.1162414	0.8974794	9.896161
GeO$_2$ [1.18]	0.68671749	0.072675189	0.43481505	0.11514351	0.89656582	10.002398

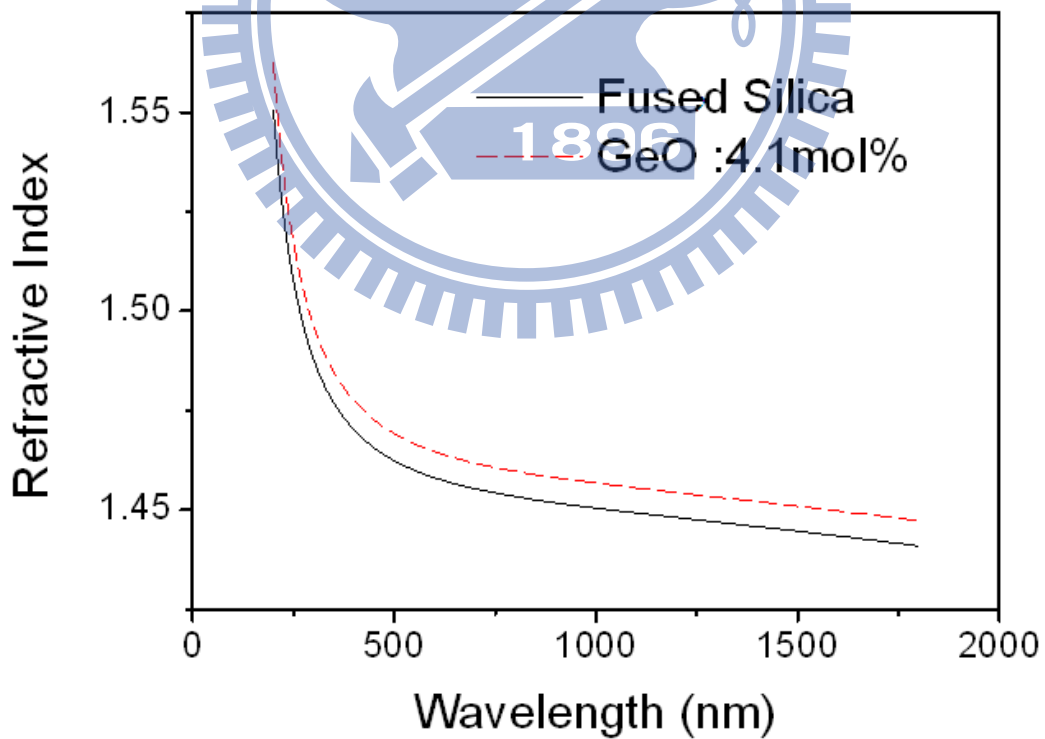Table 2.1 Sellmeier parameters used in Fig. 2-4

Fig. 2.4 Sellmeier and Cauchy's refractive index dispersion curves.

2.4-2 Waveguide Dispersion

In contrast to material dispersion, the waveguide dispersion due to the waveguide fiber structure doesn't have apparent influence on the spectral characteristics. In fused-tapered fibers, the length, diameter, strain, bending, and dopant diffusion at the tapered region are the key issues for waveguide dispersion. In general, the variation of these parameters will mainly vary the dispersion slope of the guiding modes. Usually, people discussed the influences of waveguide dispersion on fiber devices based on special fibers [2.3-2.6].

However, the waveguide structure can also be locally changed to alter the waveguide dispersion for light propagation and the spectral responses of the fiber devices by using standard fibers [2.7, 2.8]. The electromagnetic field distribution is locally modified to vary the dispersion characteristics or to excite the higher-order modes [2.9]. Therefore, novel fiber devices can be achieved based on the variation of waveguide structure of the standard fiber in a small local area. In this dissertation, since the dispersion measurement instruments are not available in these cases, the influences of the variation of the waveguide structure on the spectral characteristics are studied instead.

2.5 Reference

[2.1] H. Malitson, "Interspecimen Comparison of the Refractive Index of Fused Silica." Journal of the Optical Society of America, vol. 55, pp. 1205-1209, 1965.

[2.2] W. Fleming, "Material Dispersion in Lightguide Glasses," Electronics Letters,vol. 14, pp. 326-328, 1978.

[2.3] Zengerle and O. Leminger, "Narrow-band wavelength-selective

directional

couplers of dissimilar single-mode fibers," J. Lightwave Technol. LT-5, 1196-1198 (1987).

[2.4] J. Chung and A. Safaai-Jazi, "Narrow-band spectral filters made of W-index and step-index fibers," J. Lightwave Technol. 10, 42-45 (1992).

[2.5] Monerie, "Propagation in doubly clad single-mode fibers," IEEE J. Quantum Electron. QE-18, 535-542 (1982)

[2.6] A. Arbore, "Application of fundamental-mode cutoff for novel amplifiers and lasers," in Optical Fiber Communication Conference OFC'05 (Optical Society of America, Washington, D.C., 2005), paper OFB4.

[2.7] K. Chen, S. Chi, S. M. Tseng, and Y. Lai, "Wavelength-tunable fiber codirectional coupler filter based on asymmetric side-polished fiber coupler with local dispersive intermediate layer," submitted to ECOC 2006 conference.

[2.8] K. Chen and S. Chi, "Influence of a holey cladding structure on the spectral characteristics of side-polished endlessly single-mode photonic crystal fibers," accepted by Opt. Lett. (2006).

[2.9] K. Furusawa, A. Malinowski, J. H. V. Price, T. M. Monro, J. K. Sahu, J. Nilsson, and D. J. Richardson, Optics Express 9, 714 (2001).

Chapter3

Experiment setup and results

In this chapter, we will introduce the instruments used in our experimental setup first. Then, we will describe the steps of producing a LPFG sample. In the experimental results, we will show the surface structure of the sample with high resolution CCD camera and the transmission spectrum measured by a tunable laser. We use a temperature controller to measure the temperature sensitivity of the LPFG samples. Some samples are also put into the higher index surrounding media like water and ethanol for studying their properties in different operating regimes. At last, we will discuss the effects of periodic surface corrugation for a single mode fiber filter (SPF) by experimental results and simulation.

3.1 Experimental setup

3.1-1 Instruments utilized in fabricating LPFG

We fabricate the studied long-period fiber gratings in use of the point-by-point writing method by CO_2 laser. In the following, we introduce the used fibers and instruments for the fabrication:

1. Fibers

The fiber we use is the standard telecommunication single-mode step-index fiber (SMF-28) from Corning Corporate. The diameters of cladding and core are 125/8.2 μm respectively. The numerical aperture of fiber is 0.13. It is important to mention that this fiber is inexpensive and readily available.

2. Laser source

The instrument of our laser source is Synrad 48 series CO_2 laser. The beam diameter is 3.5 mm and the center wavelength is 10.6 μm. The maximum power is about 25 watts, but the stability (cold start) is ±5%.

Such high power laser can even heat glass to melting state. So we should be careful when operating this instrument. Before we start to run CO_2 laser, we should put on a pair of CO_2-laser-protecting glasses for safe reasons. Then we turn on the cooling first. When the cooling is working at the appropriate temperature, then we can turn on the laser.

3. Mirrors

These reflective mirrors are utilized in the wavelength of infrared ray including the wavelength of CO_2 laser. We use mirrors to control the laser beam propagation, and most important of all let the beam propagate horizontally to avoid the beam reflecting into our eyes.

4. Shutter

We utilize a relay and the aluminum block to form a basic shutter. The relay is controlled by the voltage of power supply. When the power supply is open (12 V), the shutter will be closed; when the power is closed (0 V), the shutter will be opened. So we can control the power supply with a transistor which can be connected with the port of computer by some electric circuit design.

5. Cylindrical lens

The cylindrical lens we used is from Ronar-Smith with its efficient focusing length 5.08 mm. We can focus the laser beam to about 200 μm in the z-axis. This scale is small enough for producing LPFG with period larger than 200 μm.

6. Translation Stage

Our translation stage is from Physik Instrumente with its minimum

movement 33 nm. It can be easily connected to the computer with RS-232 port and controlled automatically.

7. Computer Program

We need to fabricate LPFG automatically by computer programs to avoid the human errors. We both control the shutter and the translation by program Labview6.1.

3.1-2 Fabrication process

Figure 3.1 shows the schematic diagram of the experimental setup. Figure 3.2 shows the photography of the experimental setup (a) the overall image (b) the fiber on the fiber holder with one end tagged with a weight. First, we turn on the power of CO_2 laser and use a rock to block the beam. We will wait about ten minutes to let the power of CO_2 laser stable. In the mean time, we remove the jacket from a single mode fiber over a section about several centimeters and clean the section with ethanol. After we have cleaned the fiber, we put it on the fiber holder which is set on the translation stage. The fiber is only fixed one end on the fiber holder and the other end is tagged with a weight about 10 grams to provide a constant tension on fiber. Then we set the parameters such as the time that the shutter opens each time and the length that the translation stage moves each time. After we have set the parameters and remove the rock, we could run the programs. When the shutter is open, CO_2 laser can write on the fiber; when it is closed, the translation stage will move to the next position.
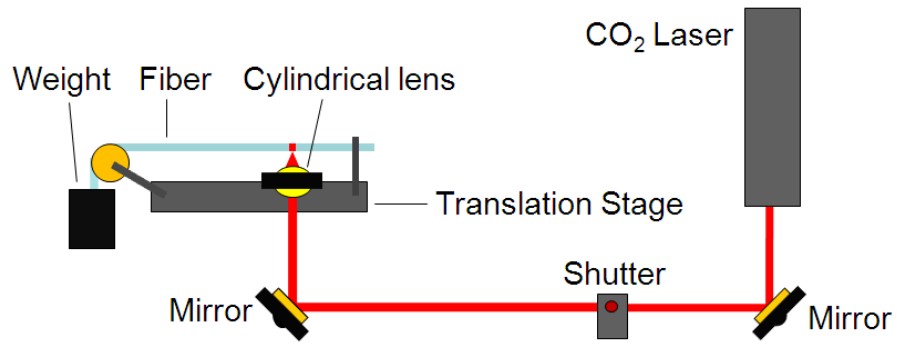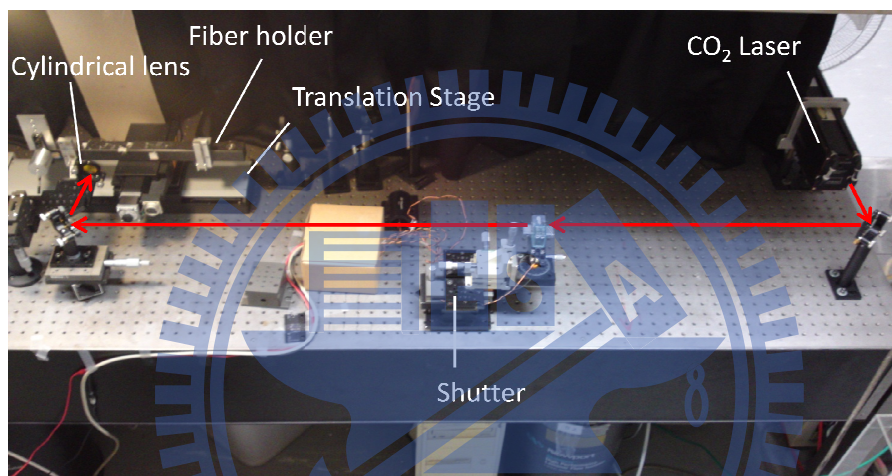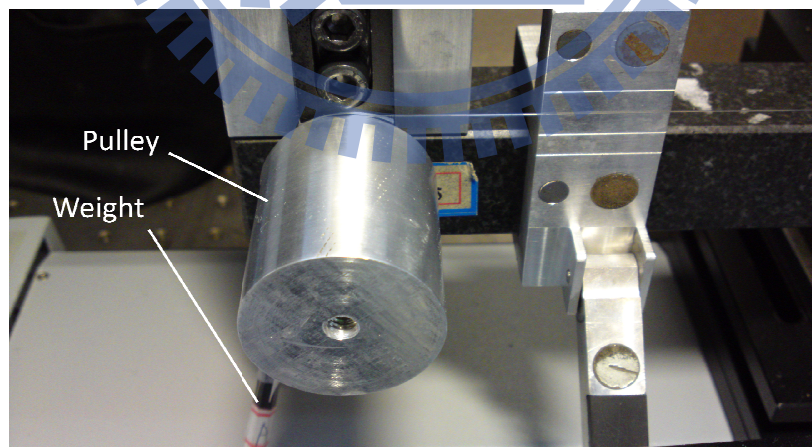
Fig. 3.1 Schematic diagram of the experimental setup for fabricating LPFG.

(a)

(b)

Fig. 3.2 The photography of the experimental setup for fabricating LPFG (a)

the overall image (b) the fiber on the fiber holder with one end tagged with a

weight.

3.2 Results and discussion

3.2-1 The surface structure observed by CCD camera

In our experiment, there are four main factors that will affect the characteristics of fabricated LPFGs, including the laser power, shutter open time, distance translation stage move each time, weight tagged on the fiber, number of the written period. If the open time of shutter is longer or the laser power is high, the higher energy heats the fiber. The heating time or the laser power for writing a fiber is related to the depth of corrugated surface structure. The distance of the translation stage moved each time determines the grating period. The tagged weight on the fiber reduces the heating time to have the same corrugated surface structure and also changes the core refractive index by residual stress relaxation. The number of written period determines the coupling length.

After we made our sample with different parameters mentioned above, we observe the surface structure by CCD camera. Figure 3.3 shows the CCD camera we use. Figure 3.4 (a) and (b) show the surface structure of LPFGs with high resolution so that we could only observe single point. Figure 3.5 (a), (b), and (c) show the surface structure of LPFGs with low resolution, and we could see the period of the grating we made.
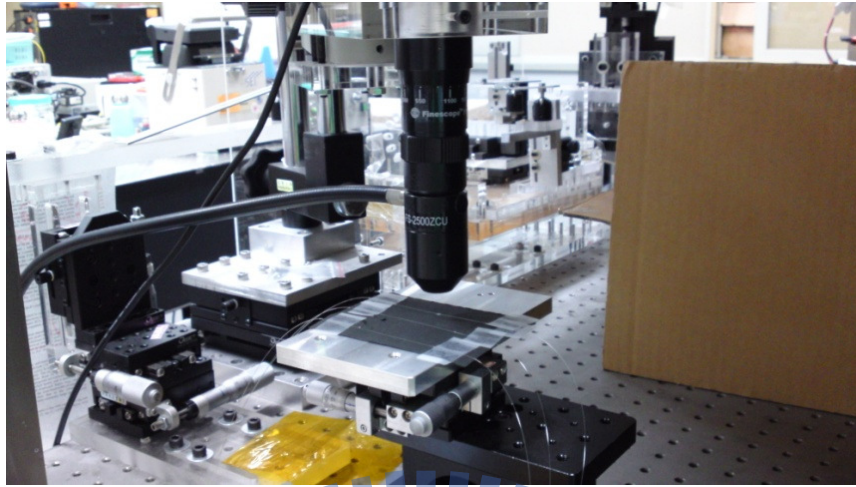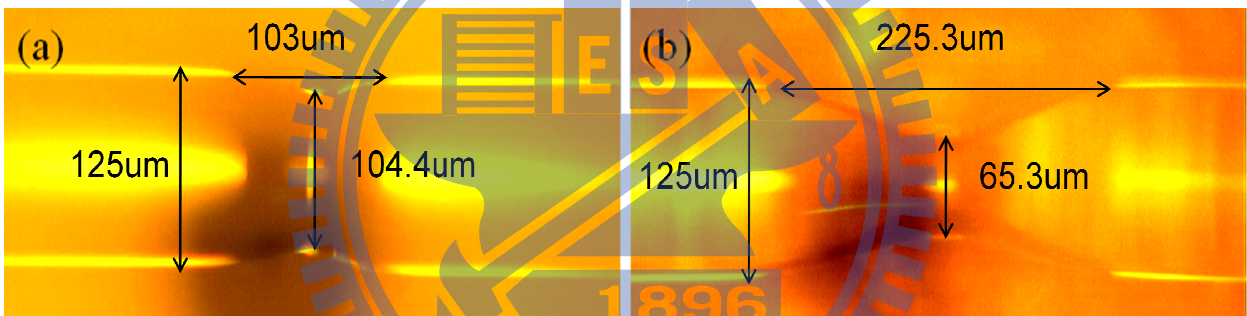
Fig. 3.3 shows the CCD camera we used.

Fig. 3.4 Optical micrograph of the periodically tapered LPFGs with (a) shallow

(waist diameter around 104.4 μm) and (b) deep (waist diameter around 65.3 μm)
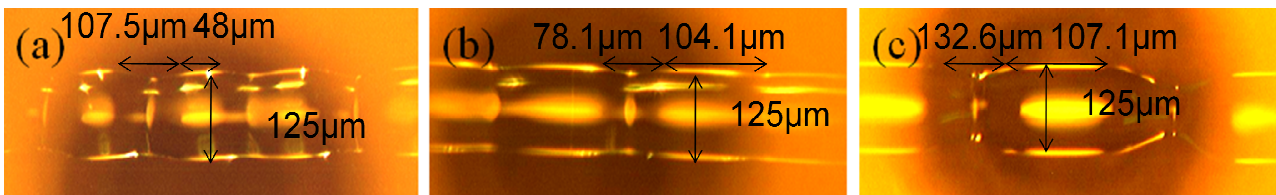
surface corrugation.

Fig. 3.5 Optical micrograph of the periodically tapered LPFGs with grating

periods of (a) 150 μm (b) 200 μm (c) and 300 μm.

3.2-2 The experiment of measurement

In our measurement, a tunable laser source from Agilent 8164A spanning from 1500 nm to 1640 nm was launched into the measured LPFG sample for performing measurement. In order to measure the sensitivity to the temperature, the LPFG sample was heated by a temperature controller to stabilize the temperature within 0.1 ℃. Also, we change the surrounding medium of different refractive index to see the effect on the transmission spectrum. We use a power sensor Agilent 81634B to observe the spectrum. Figure 3.6 shows the instruments, tunable laser and power sensor. Figure 3.7 demonstrates the transmission spectrum of the background light source.

Fig. 3.6 The instruments of tunable laser and power sensor.
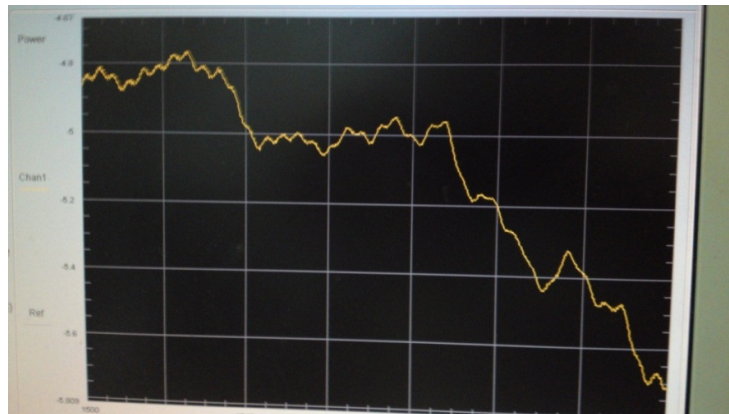

Fig. 3.7 The transmission spectrum of the background light source.

The power of background is ranged from -0.5 dBm to -1 dBm. We should subtract the background light source when we analyze the transmission spectrum of our LPFG samples.

3.2-3 The transmission spectrum of LPFGs

In the following, we will show two transmission spectrums of LPFG samples, sample1 with shallow surface corrugated structure (about 10% surface depth) and sample2 with deep surface corrugated structure (about 20% surface depth). The period and number of periods are the same for these two samples. Their period is 700μm and period number is 20 points.

We will examine the sample1 first. Figure 3.8 shows the transmission spectrum of sample1 in the air with different temperatures.
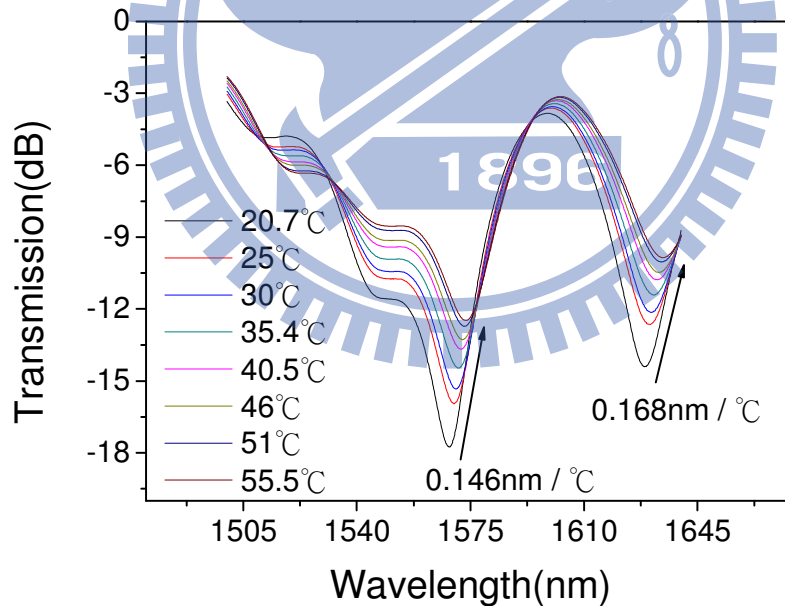

Fig. 3.8 The spectral transmission of sample1 in the air with tuning temperature ranged from 20 ℃ to 55.5 ℃.

As we can see that there are two resonance dips in figure 3.8. The insertion loss is about -3 dB, but the sensitivity for resonance dip near 1565nm is

around 0.146 nm/℃ and for resonance dip near 1625 nm is around 0.168 nm/℃. Both of them are much larger than conventional sensitivity of LPFG, which is usually 0.059 nm/℃. The depths of resonance dips are ranged from -9.5 dB to -14 dB.

We can observe that the resonance wavelength shift is almost linearly positive-dependent with the temperature of the environment while the resonance dip (dB) is linearly negative-dependent with the temperature ranged from 20 ℃ to 45 ℃. Figure 3.9 shows the relationship of resonance wavelength shift and resonance dip to the environmental temperature.
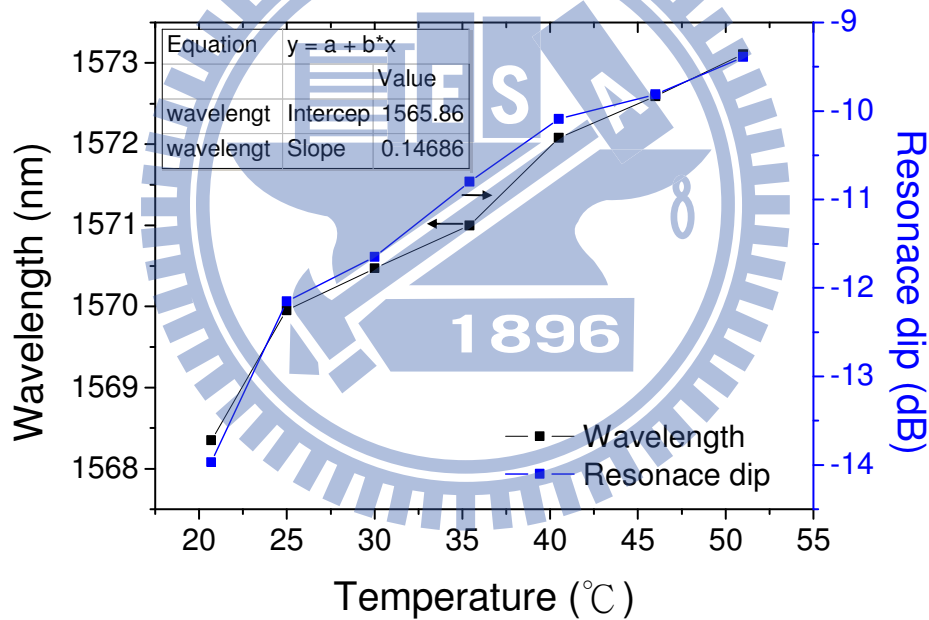

Fig. 3.9 The relationship of resonance wavelength shift and resonance dip to the environmental temperature for sample1 in the air.

In the following, we similarly show the transmission spectrum as the environmental medium changed. When we put sample1 under water, and we could see the transmission spectrum has much larger resonance wavelength shift and deeper resonance depth compared with sample1 in the air.

Figure 3.10 shows the transmission spectrum of sample1 under water with

different temperature. Figure 3.11 shows the relationship of resonance

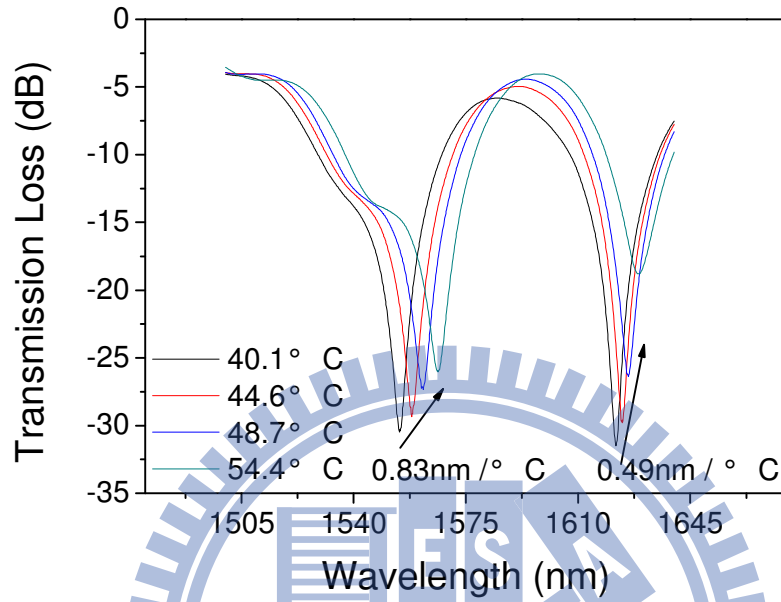wavelength shift and resonance dip to the environmental temperature.

Fig. 3.10 The spectral transmission of sample1 under water with tuning
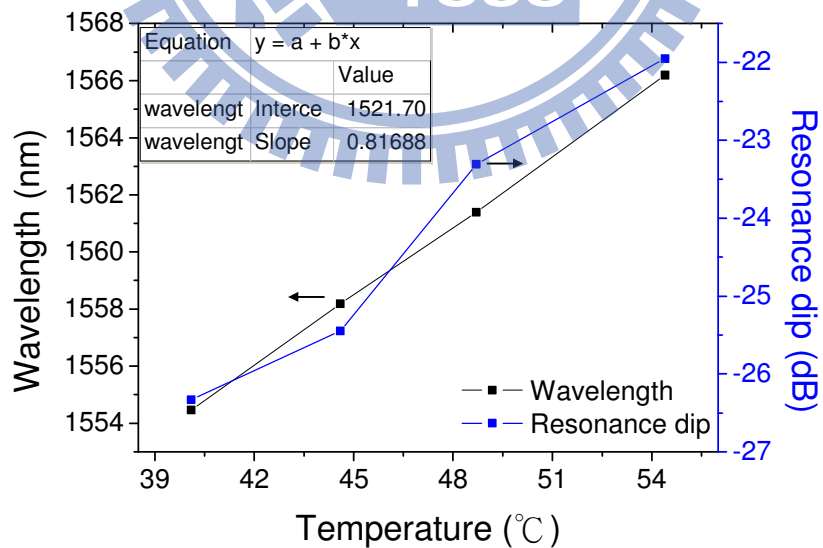
temperature ranged from 40.1 ℃ to 54.4 ℃.

Fig. 3.11 The relationship of resonance wavelength shift and resonance dip to

the environmental temperature for sample1 under water.

We then show the transmission spectrum of sample2 in the figure 3.12 and the relationship of resonance wavelength shift and resonance dip to the environmental temperature in the figure 3.12. As we can see that the insertion loss -18 dB is much larger than sample1 and the spectrum is not perfectly smooth. However, the sensitivity of the dip near 1510 nm is about 0.238 nm/℃ and is more sensitive than sample1. This higher sensitivity is probably due to the deeper surface corrugated structure. In figure 3.13, we show the relationship of resonance wavelength shift and resonance dip with respect to the environmental temperature.
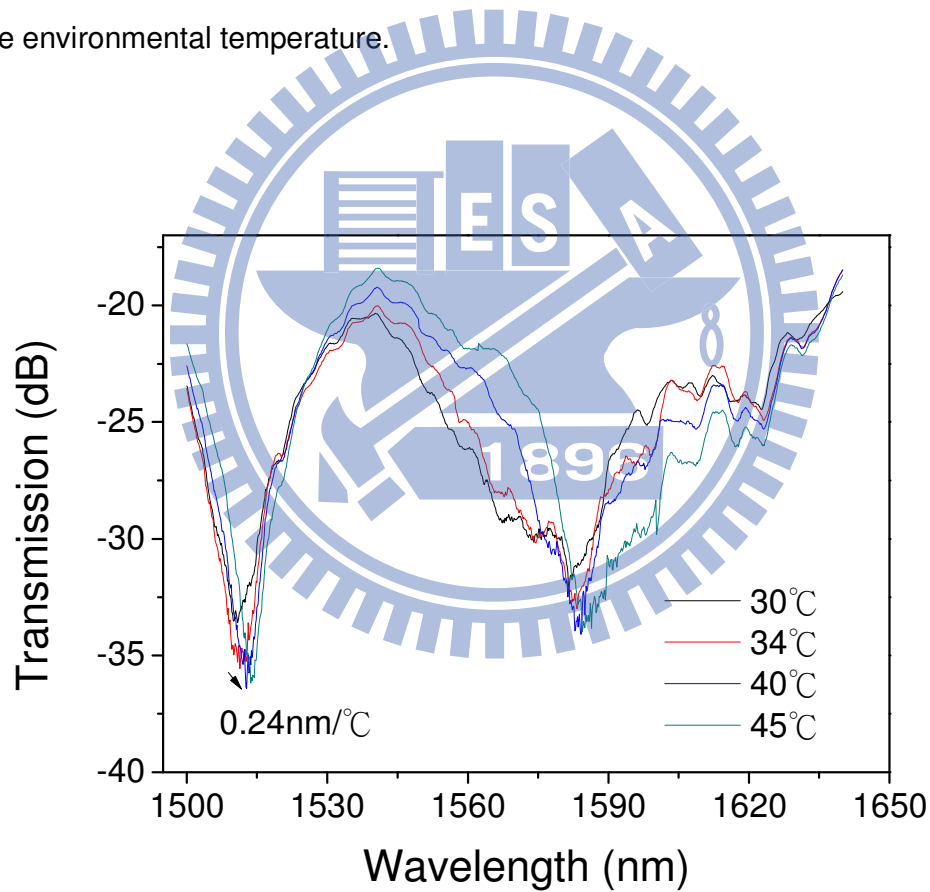

Fig. 3.12 The spectral transmission of sample2 in the air with tuning temperature ranged from 30 ℃ to 45 ℃.

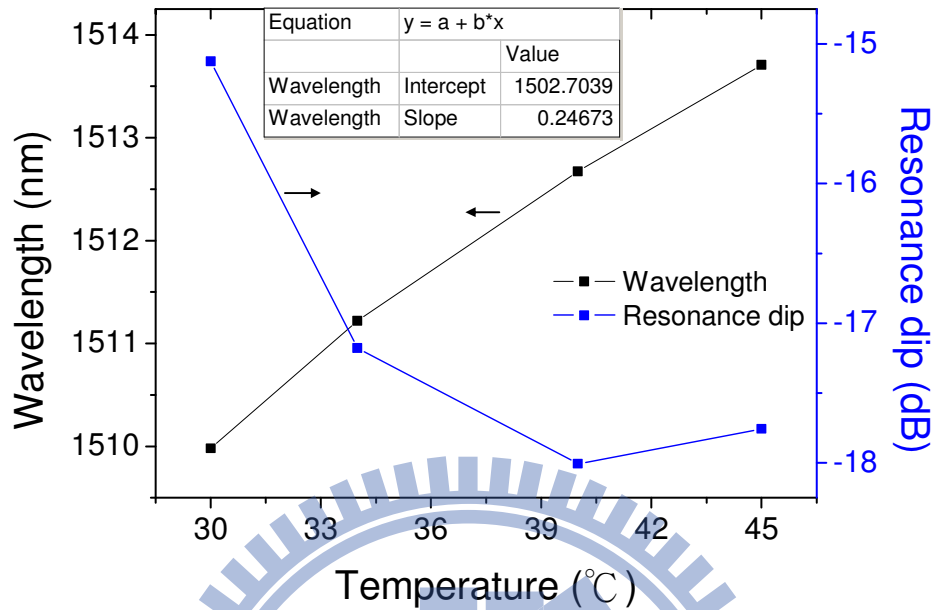| Equation	y = a + b*x	
		Value
Wavelength	Intercept	1502.7039
Wavelength	Slope	0.24673

Fig. 3.13 The relationship of resonance wavelength shift and resonance dip to the environmental temperature.

3.2-4 Discussion

We have observed that the coupling wavelength increases as the temperature increases. This is due to the change of the phase-matching condition, since the effective refractive indices of the core and cladding modes are related to the temperature and the grating period is also related to the linear thermal expansion of the single mode fiber.

The temperature sensitivity of LPFGs has been shown to be related to the environmental medium. The results show that the sensitivity of LPFG is better under water than in the air. This can be explained more fraction of field will leak to the environmental medium when the environmental refractive index is closer to the cladding refractive index. Since more fraction of field is in the environmental medium, the influence of the surrounding medium to the field is

larger. Based on the same argument, we can also explain why the sensitivity increases with deeper depth of corrugated structure. More fraction of field will leak to the environmental medium when the corrugation depth is deeper.

We have also observed that the coupling wavelength is shorter as the corrugated surface is deeper by comparing figure 3.8 with figure 3.12 and the coupling wavelength is shorter as the surrounding refractive index increases by comparing figure 3.8 and figure 3.10. According to Equation (2.5), the resonance wavelength is related to the effective index difference between fundamental mode and cladding modes, and also related to the grating period. Since the grating period is fixed for both samples, thus the decreasing resonance wavelength with increasing corrugated surface and index of surrounding media may properly due to the decreasing effective index difference of two coupling modes. In order to clarify the effective index of fiber modes, numerical simulation is performed to analyze the dispersion relation of fiber modes for specific grating periods.

3.3 Simulation

3.3-1 Assumption

We have observed the LPFG samples by a CCD camera, so the images will be limited by the resolution and aberration of the CCD camera. We can tell the diameter value of cladding by the CCD camera, but we can't tell the diameter value of core. Therefore we will assume the ratio of core diameter and cladding diameter is the same with the original SMF-28 fiber, so we can predict the diameters of core in the tapered regions.

For simplification, we use three layers of circular dielectric waveguide as the

fiber model. We change the parameters such as the indices of core, cladding, and environmental medium in our simulation. Since we only consider the modes traveling in straight waveguides, we can only tell the trend of the dips.

3.3-2 Simulation method

We use Mathematica6.0 as our simulation tool. The conditions for wave propagating in the model have been derived in equations (2.24) to (2.31), and these equations can be written as a matrix form. Since the equations are all equal to zero, the matrix is a homogeneous matrix.

We can find out effective refractive indices of core and cladding by the following steps. We use a module to calculate the determinant of the matrix and return the determinant value under particular wavelength. Plot the logarithm of the module by changing the effective refractive index shown in figure 3.14.
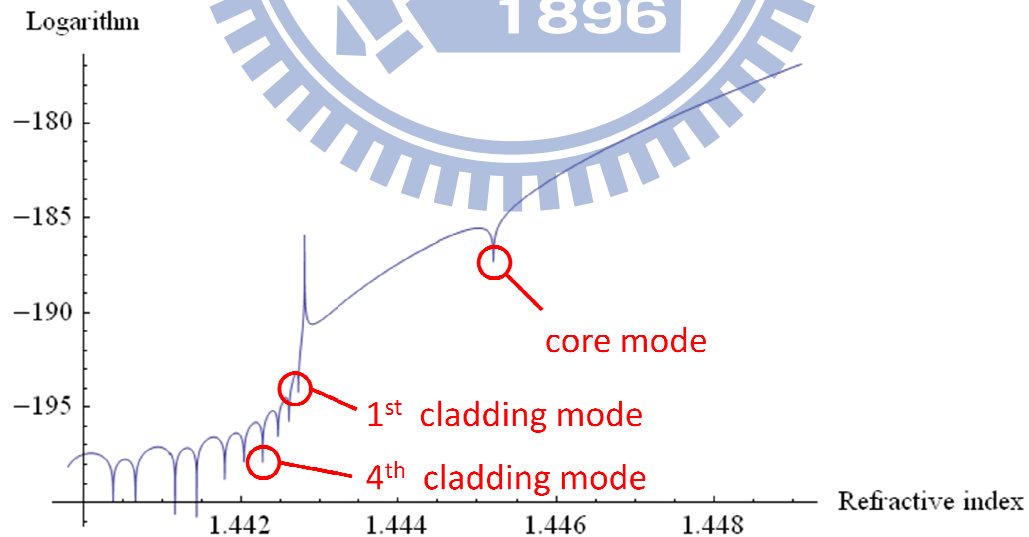

Fig. 3.14 The logarithm of the module by changing the effective refractive index.

The logarithm of roots will form a discontinuous point in the plot, and we can find out the approximate value of roots by the plot. Then we get the more accurate value of roots by Newton's method, which is the built-in command in Mathematica6.0. These roots represent the effective refractive indices of mode propagating in the model, including the core mode and cladding modes. Since the fiber we use is a single mode fiber, there should be only one core mode. In figure 3.14, we can see that there are one core mode and many cladding modes, and the effective refractive index of core mode is much higher than the cladding modes.

As stated in chapter 2, the phase-matching condition describes that

$$\frac{1}{\Lambda} = \frac{(n_{\text{eff,core}} - n_{\text{eff,cladding}})}{\lambda}.$$

We plot $1/\Lambda$ and $(n_{\text{eff,core}} - n_{\text{eff,cladding}})/\lambda$ simultaneously and the coupling wavelength can be determined by the intersection points of $1/\Lambda$ and $(n_{\text{eff,core}} - n_{\text{eff,cladding}})/\lambda$. In order to plot $(n_{\text{eff,core}} - n_{\text{eff,cladding}})/\lambda$, we need to find $n_{\text{eff,core}}$ and $n_{\text{eff,cladding}}$ under different wavelengths.

## 3.3-3 Simulation results

Simulation1

We simulate the transmission spectra with different diameters of core and cladding. Since we assume the diameters of core and cladding are in the same ratio, we denote only one of them. Figure 3.15 shows the coupling wavelength with the grating period Λ = 500 μm, 510 μm, and the air as the surrounding medium, but with different radii of core (denoted as r_{co}) (a) r_{co} = 4.1 μm, (b) r_{co} = (4.1×0.95) μm.

The slashes are $(n_{\text{eff,core}} - n_{\text{eff,cladding}})/\lambda$ for different cladding modes. M_{11}-M_{12} means the fundamental core mode coupling to the first cladding mode,

M_{11}-M_{13} means the fundamental core mode coupling to the second cladding mode, and so on. The horizontal line is $1/\Lambda$ with $\Lambda = 500\mu m$ and $\Lambda = 510\mu m$.

The intersection points are the coupling wavelengths. In figure 3.15 (a), we can observe that the wavelength of intersection points is longer when the grating period increases. The simulation result can be used to explain the red shift of coupling wavelength when the environmental temperature increases in the air.

Compare figure 3.15 (a) and (b), one can observe the coupling wavelength is shorter as the diameter of core decreases. These simulation results verify that the index difference of the two coupling modes at specific wavelength decreases with deeper surface corrugated surface, which coincides with the experimental results shown in figure 3.8 and figure 3.12.
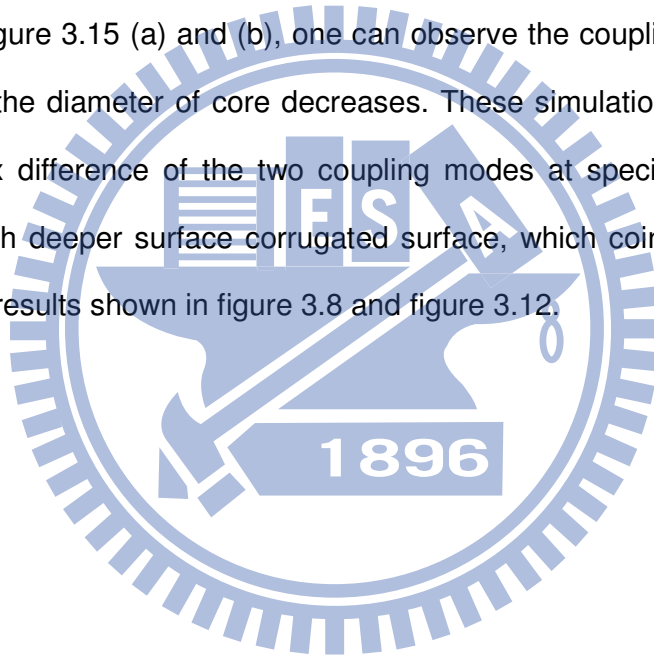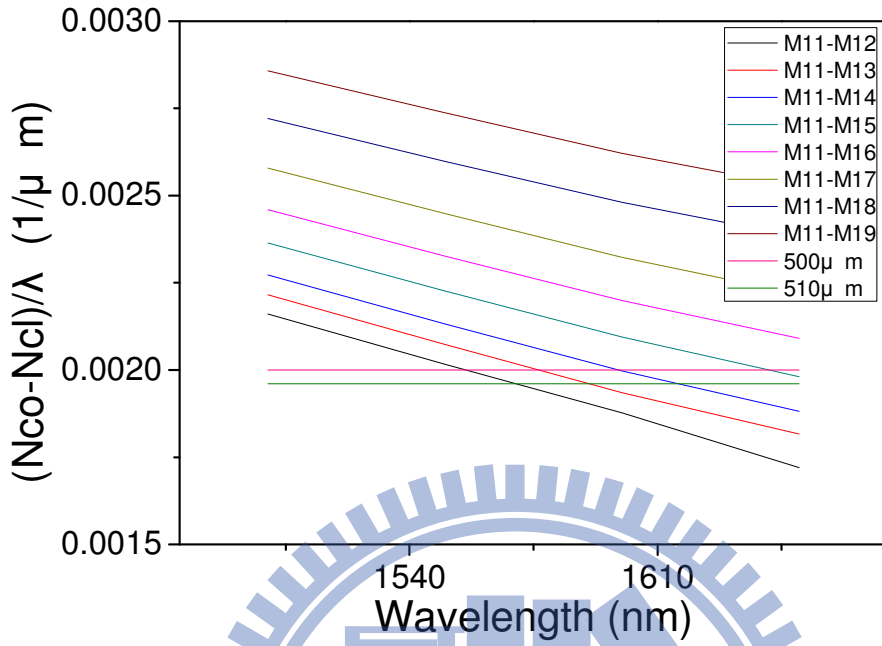
(a)
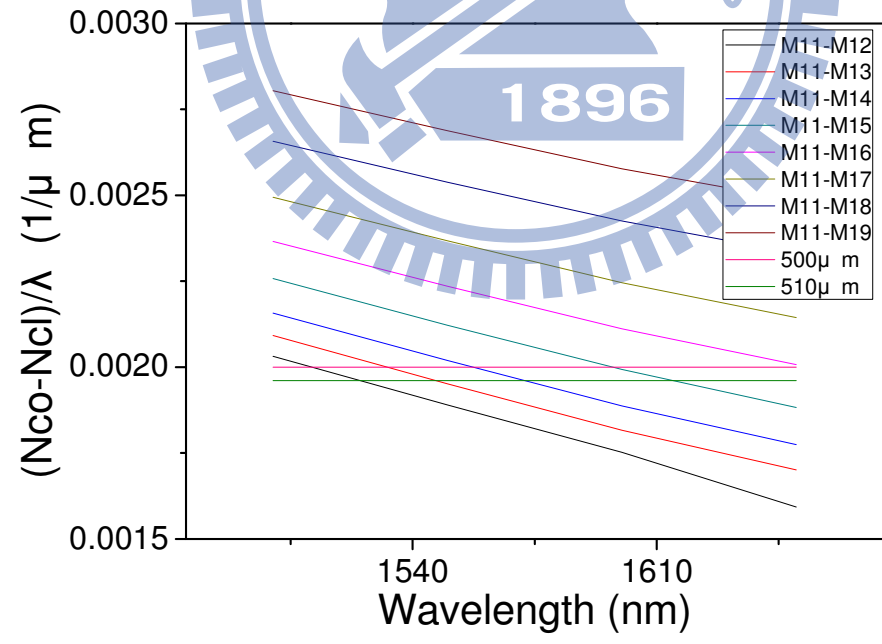
(b)

Fig. 3.15 The coupling wavelength with grating period Λ = 500μm and air as

the surrounding medium, (a) r_{co} = 4.1 μm, (b) r_{co} = (4.1×0.95) μm.

Simulation2

In the above simulation, we consider the changing diameters of core and cladding. In the following, we subtract the index of core a small number to study the corresponding changes.

Figure 3.16 shows the coupling wavelength with the grating period Λ = 500 μm and the core index change Δn_{co} = -5×10^{-4}. Comparing figure 3.16 and figure 3.15 (a), the coupling wavelength is shorter as the core index decreases.
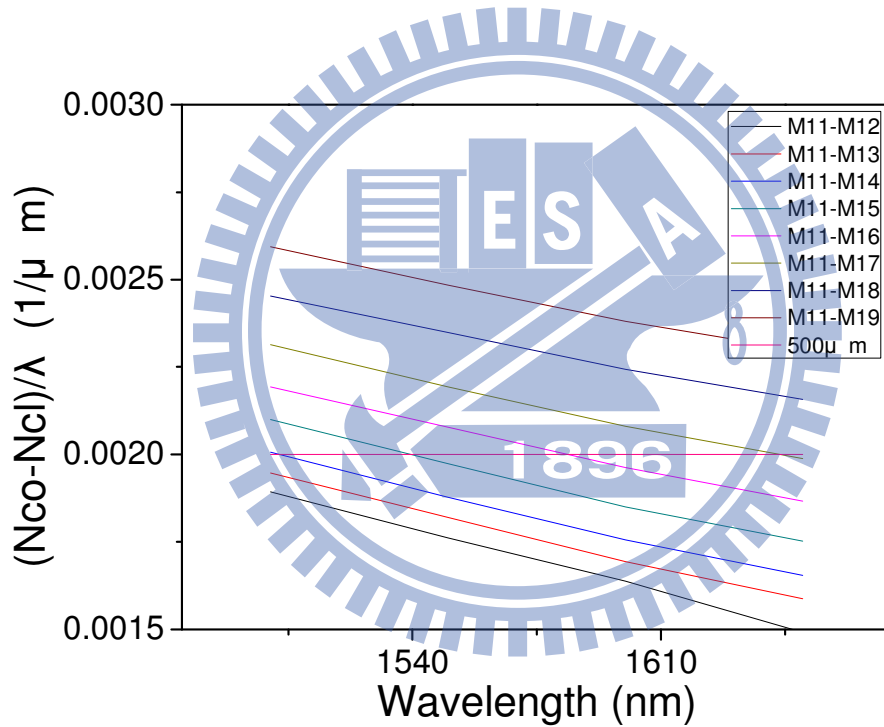

Fig. 3.16 The coupling wavelength with grating period Λ = 500 μm and the change of core index Δn_{co} = -5×10^{-4}.

Simulation3

In this simulation we consider both the parameters of the diameter and core index. We set the diameter of core to be 90% of SMF-28 and the change of

core index $\Delta n_{co} = -5 \times 10^{-4}$. Figure 3.17 shows the simulation results with grating period Λ = 700µm.

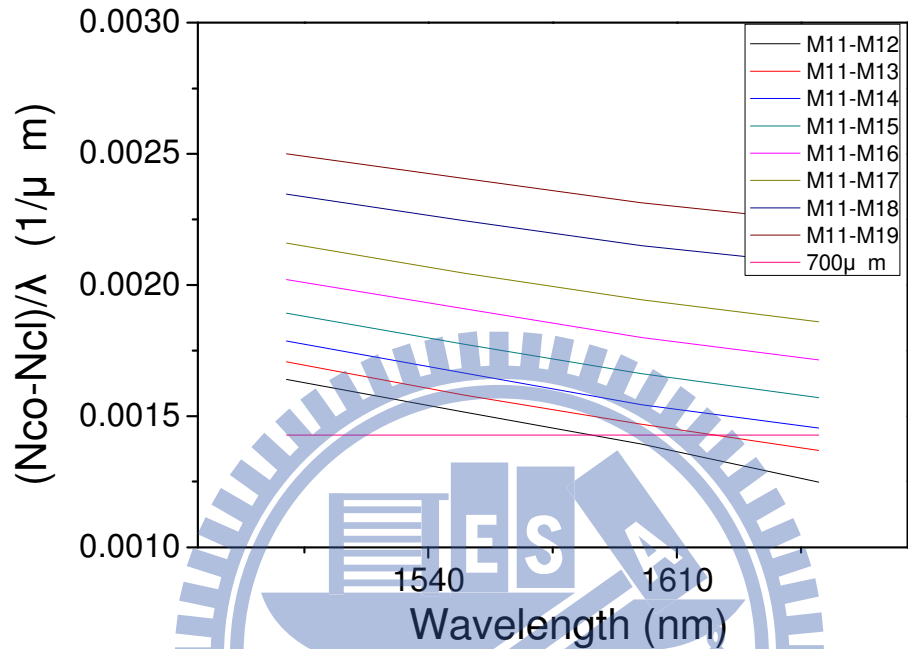Fig. 3.17 The coupling wavelength with grating period Λ = 700µm,

r_{co} = (4.1×0.9) µm and Δn_{co}= -5×10⁻⁴.

In figure 3.17, the coupling wavelengths are near 1580nm and 1620nm. It's quite similar to sample1 even though we use such a simple model.

Next, we set the diameter of core to be 80% of SMF-28 and the change of core index $\Delta n_{co} = -5 \times 10^{-4}$. Figure 3.18 in the next page shows the results with the grating period Λ = 700µm. It's also quite similar to the experimental results of sample2.
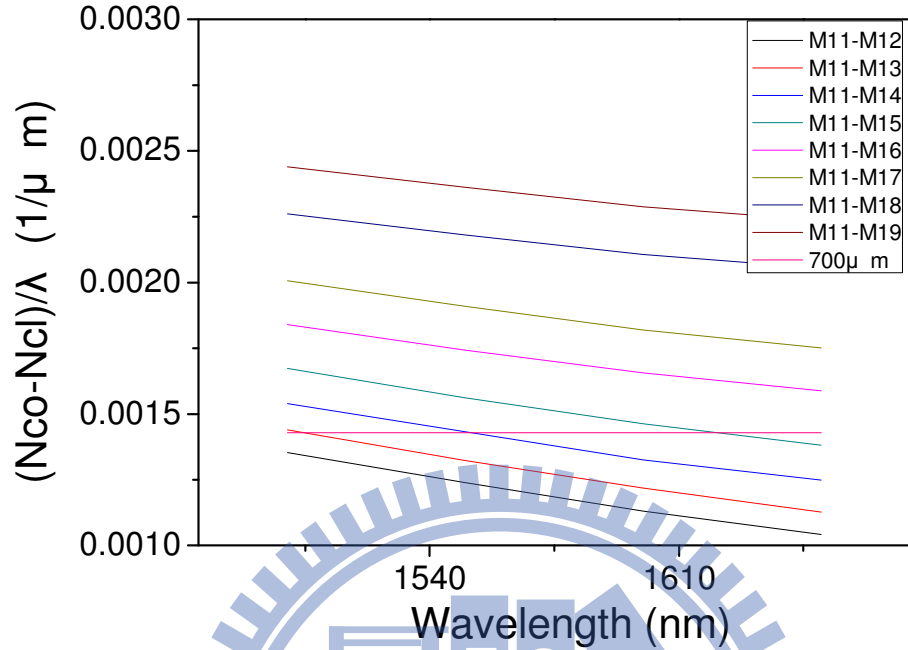
Fig. 3.18 The coupling wavelength with grating period $\Lambda = 700\mu m$,

$r_{co} = (4.1 \times 0.8)$ μm and $\Delta n_{co} = -5 \times 10^{-4}$.

3.4 Possible improvement of the fabrication process

The obtained results could be better if we could make some improvements in our fabrication method. First, the period is not very good under CCD camera and some of the points are deeper and some of them are shallower. The non-uniformity may cause large insertion loss in the transmission spectrum.

There are two reasons for causing the non-uniformity of the LPFGs: the instability of CO_2 laser and the rough design of shutter. The CO_2 laser we use has ±5% error, but we can open air conditioners to help laser more stable. The shutter is designed by a delay, which has problems when the switching time interval is short. When the heating time is short, this shutter is not accurate

enough. Also, I have found that the transmission power passing through the shutter is not equal each time. This may be the main reason that was causing the non-uniformity. Better results can be expected by using a better shutter with short response time and the same transmission power.
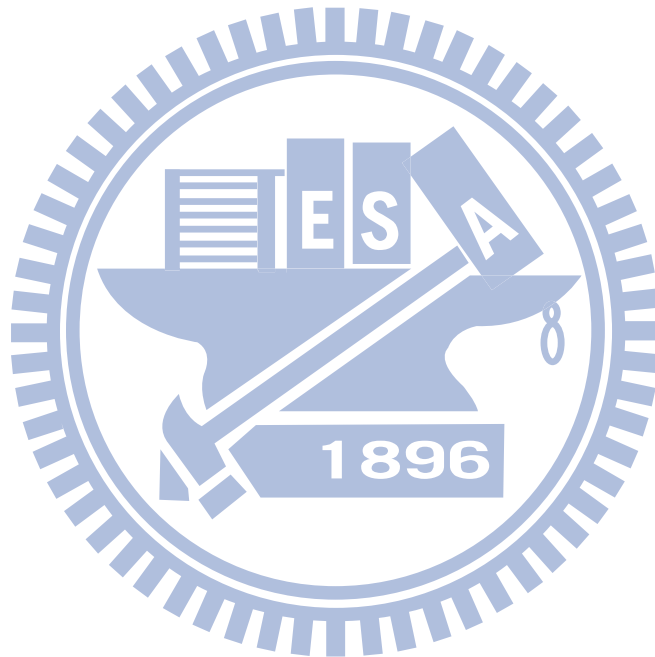
# Chapter4

Conclusions and Future Work

4.1 Conclusions

The LPFGs with periodically tapered structure have been demonstrated with higher sensitivity than the conventional LPFGs which are usually 0.059 nm/℃. The sensitivity of sample1 in the air is 0.146nm/℃, and it is almost three times of the conventional LPFGs. The sensitivity of sample2 in the air is 0.238 nm/℃, and it is about four times of the conventional LPFGs. The main difference of sample1 and sample2 is the depth of surface structure of optical fiber. Since sample2 is deeper than sample1, we can conclude that this structure improve the sensitivity of LPFGs. We can reach higher sensitivity when LPFGs are in the higher index medium such as water. The sensitivity of sample1 in the water can reach 0.83nm/℃, which is almost six times in the air.

In simulation, we have verified the parameters such as the diameter of fiber and core refractive index will affect the coupling wavelength. When the depth of surface structure becomes deeper or core index decreases, the resonance dip moves to the shorter wavelengths. The simulation results can explain the trend of the experimental results: the resonance wavelength exhibits red shift as temperature increases. By considering both the effects of surface structure and the change of core refractive index, we also can get similar resonance wavelengths that can be compared to the experimental transmission spectra of our LPFG samples.

4.2 Future Work

First we should improve our LPFG performance such as decreasing insertion loss and increasing the yield rate. In the future, we can apply the LPFGs as a fiber device, since we know how parameters will change the transmission spectrum of LPFGs. It is convenient not only to produce the transmission spectrum we want but also easy to tune the coupling wavelength finely by utilizing temperature controllers.

For further study of LPFGs, we can try to improve the sensitivity of LPFGs or produce new structure of LPFGs. We can try to coat a layer of polymer on the LPFGs or change different surrounding media.
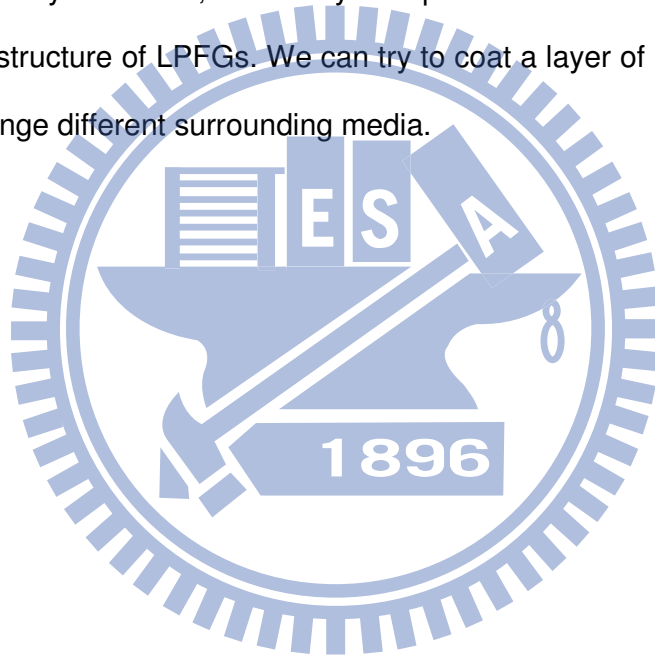
Vita

姓名：呂柏萱

出生地：台灣　新竹市

學歷：國立科園實驗國小

　　　新竹市立建華國民中學

　　　國立科園實驗高中

　　　國立交通大學電子物理學系

　　　國立交通大學顯示科技研究所